

Kinetics of Li transport in vanadium-based disordered rocksalt structures

Zinab Jadidi^{1,2}, Tina Chen^{1,2}, Luis Barroso-Luque^{1,2}, Gerbrand Ceder^{1,2}

¹ Department of Materials Science and Engineering, Berkeley CA 94720

² Materials Sciences Division, Lawrence Berkeley National Laboratory, Berkeley CA 94720

Abstract - Disordered rocksalt Li-excess (DRX) compounds have emerged as promising new cathode materials for lithium-ion batteries, as they can consist solely of resource-abundant metals and eliminate the need for cobalt or nickel. A deeper understanding of the lithium-ion transport kinetics in DRX compounds is essential for enhancing their rate performance. This study employs first-principles calculations, cluster expansion techniques, and kinetic Monte Carlo simulations to investigate the Li⁺ transport properties in DRX Li_{2-x}VO₃, where 0 ≤ x ≤ 1. Our findings underscore (i) the necessity of accounting for both tetrahedral and octahedral Li occupancy when predicting the transport properties in DRX materials, (ii) the factors influencing the variation in the diffusion coefficients with Li content in Li_{2-x}VO₃, and (iii) the impact of Li⁺ correlated motion on the kinetics of Li⁺ transport. We reveal that the relative stability of tetrahedral and octahedral Li determines the number of active sites within the percolation network, subsequently affecting the Li⁺ transport properties. Furthermore, we demonstrate that the wide site-energy distribution causes correlated motion in Li_{2-x}VO₃, which hinders Li⁺ transport. Although our study focuses on Li_{2-x}VO₃ as a model system, the insights gained apply to all DRX materials, given their inherently broader site-energy distributions.

INTRODUCTION

Disordered rocksalt cathodes were initially considered electrochemically inactive (1,2) due to the slow kinetics of Li⁺ transport, resulting in subpar electrochemical performance. (3) However, the development of the so-called zero-transition-metal (0-TM) percolation theory facilitated the design of disordered rocksalt materials with improved Li⁺ transport properties. (4,5) The 0-TM percolation theory (4,5) was developed based on the concept of octahedral Li occupancy and the tetrahedral site hop (TSH) diffusion mechanism. (6) In this mechanism, a Li⁺ migrates from an octahedral site to an adjacent (edge-sharing) octahedral site via an intermediate tetrahedral site without any TM in the neighboring face-sharing octahedral site (0-TM channel). (4,5) According to the 0-TM percolation theory, Li⁺ in a disordered structure can percolate if there is sufficient Li (an excess beyond the 1:1:2

Li:TM:O ratio of typical ordered rocksalt cathodes) to form low-barrier percolating 0-TM diffusion networks. (4,5) As disordered rocksalt structures with Li-excess (DRX) materials can be designed with a broader range of elements (4,7–16), the insights gained from the 0-TM percolation theory have provided valuable guidelines for the battery community. This has led to the development of cobalt-free and nickel-free DRX cathode materials capable of delivering specific energies up to 1000 Wh/kg. (3,7)

Although the 0-TM percolation theory offers valuable insights into the structural features that can influence Li⁺ transport properties, it does not include all the factors affecting transport. As a result, its predictions do not always lead to high Li diffusivity (11,12,17) or the desired rate performance. (18) For instance, Li₂VO₂F exhibits considerable Li-excess but it is reported to have capacity fade due to seemingly slow Li⁺ transport kinetics. (18)

A significant aspect not addressed in the current 0-TM percolation theory is the possibility of Li occupying tetrahedral sites in DRX materials (19–21), particularly in highly delithiated states where non-face-sharing tetrahedral Li sites can form. Consequently, alternative Li⁺ hopping mechanisms, such as hops from a tetrahedral site to another tetrahedral site through an octahedral site or from an octahedral/tetrahedral site to a tetrahedral/octahedral site (20,21), are not considered in the 0-TM percolation analysis of DRX materials.

Another crucial aspect not included in the current percolation theory is the variability of the site energy which may lead to highly correlated Li⁺ motion, and hereby significantly hinder transport. (6,22,23) For instance, even if a network of low-barrier pathways exists, the Li⁺ motion may be correlated in such a way that it moves in circles or hops back and forth between the same sites, resulting in no net transport despite locally low migration barriers. (22,23) This type of highly correlated Li jumps have been shown to impede Li⁺ transport in spinel Li_xTiS₂ (22) despite its fully connected 0-TM network.

To expand our understanding of the critical factors influencing Li⁺ percolation in DRX materials, we develop a kinetic model that accounts for both tetrahedral and octahedral Li occupancy and the variable site energies of Li due to the diversity of local environments. In this paper, we study Li_{2-x}VO₃, where 0 ≤ x ≤ 1, as a model system that has

been investigated as a potential cathode material (24). We model this system using a lattice cluster expansion, fit to density functional theory (DFT) first-principles calculations, that includes quaternary disorder ($\text{Li}^+/\text{V}^{4+}/\text{V}^{5+}$ and vacancies) on octahedral sites and binary disorder (Li^+ and vacancies) on tetrahedral sites. The kinetics of Li^+ transport is modeled with this cluster expansion using the kinetic Monte Carlo method, employing the rejection-free (n-fold) algorithm. (25) Our findings reveal that the relative stability of the tetrahedral sites compared to the octahedral sites plays a crucial role in determining how Li^+ diffusivity varies with Li content. Furthermore, we demonstrate that the wide site energy distribution is the primary factor behind the correlated motion in $\text{Li}_{2-x}\text{VO}_3$. Our analysis recognizes a flat energy landscape as a critical design criterion for improved transport in DRX materials.

METHODS

A. Cluster expansion model

The cluster expansion (CE) method provides a formal representation of the energy landscape with respect to the configuration of species located on a predefined topology of lattice sites. (26–28) Extensive configurational sampling can be obtained by using Monte Carlo with the CE method, which is not possible directly using DFT. The CE model used in this work was constructed using the Statistical Mechanics on Lattices (smol) Python package (29) and was extensively described in our previous work on the cationic short-range ordering of $\text{Li}_{2-x}\text{VO}_3$, $0 \leq x \leq 1$. (30) We present a brief overview of our model and refer readers to the aforementioned references for further details.

The CE for the configurational energy is written in the form shown in equation 1:

$$E(\boldsymbol{\sigma}) = \sum_{\beta} V_{\beta} \langle \Phi_{\alpha}(\boldsymbol{\sigma}) \rangle_{\beta}. \quad (1)$$

The occupancy string $\boldsymbol{\sigma}$, in which each element σ_i denotes an occupation variable for site i , is used to represent configurations. The summation in equation 1 encompasses all symmetrically distinct clusters of basis functions β . We use sinusoidal basis functions as detailed by Van de Walle et al. (31) The coefficients V_{β} are the effective cluster interactions (ECI) weighted by the crystallographic multiplicity of the corresponding clusters. (26,32) The functions Φ_{α} are cluster functions. (31)

Our CE model considers pair interactions up to 7.1 Å and triplet interactions up to 4 Å, based on a cubic cell with a lattice constant $a = 3.0$ Å. An Ewald summation term is also included in the energy model to increase the accuracy and sampling stability of our CE by accounting for long-range electrostatic interactions. (15,33–35)

The degrees of freedom in the lattice model for $\text{Li}_{2-x}\text{VO}_3$, as illustrated in Figure 1, include $\{\text{Li}^+, \text{V}^{4+}, \text{V}^{5+}, \text{vacancy}\}$ on the octahedral sublattice (24) and $\{\text{Li}^+, \text{vacancy}\}$ on the tetrahedral sublattice. (19,21) The anion sites are fully occupied by O^{2-} and hence do not need to be represented in the CE. (24) Sparse group lasso regularization was used to fit

the ECIs of this high-component system using DFT energies of 450 symmetrically distinct configurations. In 10-fold cross-validation the resulting fit reproduced DFT with a root-mean-squared error (RMSE) of 13.1 meV per site and in-sample RMSE of 12.4 meV per site.

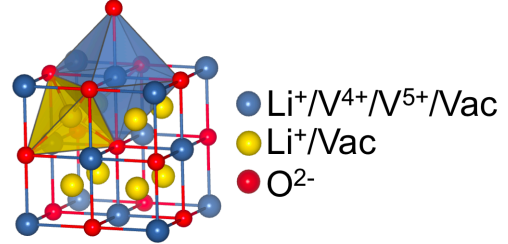


FIG. 1. Rocksalt lattice of $\text{Li}_{2-x}\text{VO}_3$, $0 \leq x \leq 1$. The blue spheres correspond to the face-centered cubic (FCC) lattice of octahedral sites, which can be occupied by Li^+ , V^{4+} , V^{5+} , or a vacancy. The yellow spheres correspond to tetrahedral sites, which can be occupied by Li^+ or a vacancy. The red spheres form the anion lattice, which is fully occupied by oxygen and does not need to be included in the degrees of freedom of the CE.

B. First-principles DFT calculations

The structure–energy dataset used to fit the CE was obtained using DFT (36,37) implemented in the Vienna ab-initio simulation package (VASP) (38,39) with the projector-augmented wave (PAW) method. (40,41) The PBE exchange–correlation functional (42) with rotationally averaged Hubbard ($U = 3.1$ eV) correction was used based on a previously reported calibration to oxide formation energies (3.1 eV for V). (15,43) A plane-wave cutoff of 520 eV, reciprocal-space discretization of 25 K-points per Å, electronic convergence of 10^{-5} eV and 0.01 eV Å $^{-1}$ for forces were used in all of our calculations.

The Nudged Elastic Band (NEB) calculations are conducted using five images along the diffusion paths for single-vacancy and divacancy tetrahedral site hop (TSH) mechanisms at compositions of LiVO_3 , $\text{Li}_{1.5}\text{VO}_3$, and Li_2VO_3 in supercells of $3 \times 3 \times 3$ or $3 \times 4 \times 3$, containing 27 or 36 oxygen atoms. Configurations for the NEB calculations are created by Monte Carlo at temperatures of 300 K and 5000 K to generate various local environments for Li^+ migration. In the NEB calculations, it is ensured that the distance between the migrating Li^+ and its periodic image exceeds 8 Å in order to prevent any interaction between periodic images. All the NEB calculations are performed using the GGA method without the Hubbard-U correction to prevent potential convergence issues arising from electron localization at different atomic centers along the migration path. (44,45)

C. Transport properties

In solid crystalline intercalation compounds, such as DRX materials, the diffusion of Li^+ typically occurs through a substitutional diffusion mechanism, in which Li^+ migrates to adjacent vacant sites. (6,22,46–49) The presence of diverse local environments in DRX materials results in a dependency of the Li^+ migration energy barrier on its local surroundings. Kinetic Monte Carlo (KMC) simulations can combine a cluster expansion to incorporate the $\text{Li}^+ - \text{Li}^+$ and Li^+ -host energetics with a local cluster expansion to model the

variations in migration energy. (6) We show below a simplified model to capture the dependence of migration energy on environment.

To derive the diffusion coefficients from the Li trajectories we employ the Green-Kubo approach, derived from the fluctuation theorem at equilibrium. (50–52) The chemical diffusion coefficient, $D_{Chemical}$, represents the relationship between the flux of migrating species, and their concentration gradients. (51) $D_{Chemical}$ can be calculated by multiplying the thermodynamic factor, Θ , with the jump diffusion coefficient, D_{Jump} (51):

$$D_{Chemical} = \Theta D_{Jump}. \quad (2)$$

The thermodynamic factor Θ , given by equation 3, measures the deviation of the solution thermodynamics from the non-interacting ideal solution. When Li^+ - Li^+ interactions are negligible (in the dilute-limit case), the thermodynamic factor is equal to 1.

$$\Theta = \frac{\partial \left(\frac{\mu}{k_B T} \right)}{\partial \ln(x)}. \quad (3)$$

In equation 3, μ represents the Li chemical potential, k_B denotes Boltzmann's constant, T signifies the absolute temperature, and x corresponds to the Li concentration. Because μ is the negative of the cathode voltage (53) the thermodynamic factor is related to the voltage profile. In this study, the thermodynamic factor is computed by scanning the Li chemical potential in steps of 0.05 eV using semi-grand canonical Monte Carlo (SGC MC) simulations at $T = 300$ K. The thermodynamic and transport analysis are conducted in a $9 \times 8 \times 9$ supercell (comprising a 648-oxygen supercell) of $\text{Li}_{2-x}\text{VO}_3$ with Li/V metal configurations obtained by equilibrating at 1800 K. The selection of 1800 K was established in previous work and is based on the similarity of the simulated and experimental voltage profiles and XRD patterns at this temperature. (30)

The jump diffusion coefficient D_{Jump} in equation 2 measures the fluctuation of the center of mass of all diffusing Li-ions and can be determined as (54,55):

$$D_{Jump} = \frac{1}{2dt} \frac{1}{N} \left\langle \left[\sum_{i=1}^N \Delta \vec{R}_i(t) \right]^2 \right\rangle. \quad (4)$$

In equation 4, d represents the dimension of the lattice on which diffusion occurs (for DRX $\text{Li}_{2-x}\text{VO}_3$, d is 3), t denotes time, N refers to the number of diffusing Li ions, and $\Delta \vec{R}_i(t)$ is the displacement vector of the i th ion after time t . The angular brackets signify the ensemble average after time t .

Compared to D_{Jump} , the tracer diffusion coefficient, D_{Tracer} , is based on the fluctuation of the position of individual Li-ions and can be determined as follows:

$$D_{Tracer} = \frac{1}{2dt} \frac{1}{N} \sum_{i=1}^N \left\langle [\Delta \vec{R}_i(t)]^2 \right\rangle. \quad (5)$$

The tracer diffusion includes self-correlation caused by the diffusion topology and the energy landscape. The deviation of D_{Tracer} from the random-walk scenario is measured by the correlation factor : (22)

$$f = \frac{\langle \vec{R}(t)^2 \rangle}{na^2}. \quad (6)$$

In equation 6, $\langle \vec{R}(t)^2 \rangle$ represents the mean squared displacement of a Li ion after a time t . The variable n refers to the number of jumps Li^+ has executed during the simulation period, and a is the hop distance.

The rate constants Γ_{ij} for Li^+ hopping from site i to site j can be determined from transition state theory (56):

$$\Gamma_{ij} = \nu^* \exp \left(-\frac{\Delta E_{ij}}{k_B T} \right). \quad (7)$$

where ν^* is the vibrational prefactor, estimated to be 10^{13} . (6) The migration activation barrier for Li^+ hopping from site i to site j is represented by ΔE_{ij} . As ΔE_{ij} depends on the local environment, it is crucial to parameterize its value in accordance with the variations in these local environments. (6,47,49)

When tetrahedral Li sites can be occupied, more elementary diffusion steps are possible than when Li only occupies octahedral sites. (21) To simplify our kinetic model, we allow Li^+ to hop between octahedral sites and their nearest-neighbor (face-sharing) tetrahedral sites and vice versa, as most of the diffusion mechanisms in DRX materials (21) can be broken down into these two fundamental hops. Hence, we assign a value of 1.82 Å to parameter a in equation 6, as it corresponds to the nearest-neighbor distance between octahedral and tetrahedral sites. Li^+ migration in DRX compounds can also potentially occur directly from a tetrahedral site to an edge-sharing tetrahedral site. (21) However, we have excluded this mechanism for two reasons. Firstly, the barrier for Li^+ migration through edge-sharing tetrahedral-tetrahedral hops has been found to reach up to 900 meV. (21) Secondly, including this mechanism will not significantly impact our simulation's final results since most low-barrier Li^+ migration mechanisms predominantly occur through the triangular face rather than the edge. (21)

The energy of a Li^+ ion in a tetrahedral site depends strongly on the occupancy of its four face-sharing octahedral sites. In our kinetic model, we account for all Li^+ transitions from octahedral to tetrahedral sites that do not face-share with any vanadium-occupied sites, or face-share with a single vanadium-occupied site and two vacant sites. These transitions are abbreviated as 0-TM and 1-TM_{di-vac} in line with notation in earlier papers on diffusion in rocksalt-like materials. (4,5) Due to the high migration energy observed in the 1-TM_{single-vac} hop (Figure S1), we omitted it from our KMC simulations. Hops into tetrahedral sites with two face-sharing vanadium have even higher energy and can be excluded from our simulation.(4) Migration barriers for face-sharing hops are obtained from NEB calculations of the TSH mechanism when the tetrahedral site represents a local minimum in the minimum energy pathway. To integrate migration barriers with the site energy landscape of the cluster expansion, we use the kinetically resolved activation (KRA) barrier in KMC simulations as originally proposed by Van der Ven. (6) The KRA is calculated by subtracting the average energy of the hop's endpoints from the energy of the activated

state. (6) In our KMC simulations, we employed a single KRA value for all hops, and we provide the rationale for this decision in Figure 2.

KMC simulations are conducted at 300 K using the rejection-free algorithm. (57,58) The initial state of each KMC simulation is done in a $9 \times 8 \times 9$ supercell for 12 compositions of $\text{Li}_{2-x}\text{VO}_3$. At each KMC step (i.e., a Li^+ hop to a nearby vacancy), we randomly select a migrating Li^+ and choose a jump based on a probability proportional to its rate. (25) We perform 50,000 KMC steps starting from each initial configuration and average the Li^+ trajectories after 20,000 steps to ensure the system is fully equilibrated.

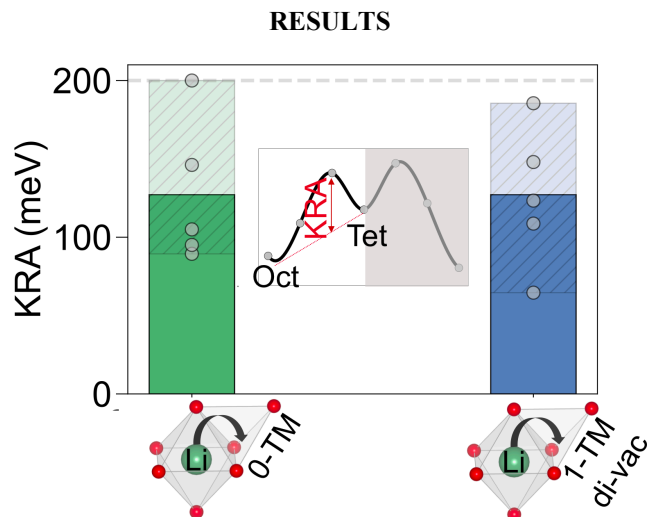


FIG. 2. The KRA barriers for Li^+ hops from an octahedral site to 0-TM (green) and 1-TM_{di-vac} tetrahedral sites (blue) are displayed. The solid bars represent the average value of the KRAs, and the hatched bars illustrate the range between the maximum and minimum values of the KRAs for each hop category. These KRAs were determined from 10 NEB calculations of TSH mechanisms on different Li/V configurations. In these calculations, the intermediate tetrahedral site acts as a local minimum for the migrating Li^+ (as shown in the inset plot). The circle markers indicate the data points for each hop category. The gray dotted line represents the upper limit of the KRA

values, set at 200 meV, which is used as input for all octahedral-to-tetrahedral (or vice versa) hops in the KMC simulation.

Figure 2 displays the KRA values for Li^+ hops from octahedral sites into a tetrahedral site face-sharing with different number of TM's and vacancies. Values are plotted for a tetrahedron with no TM face-sharing and either 1, 2 or 3 vacancies (green) and for the single -TM face-sharing with 2 vacancies (blue). The minimum energy pathways for all 10 NEB calculations used to determine the KRA values are presented in Figure S2.

The KRA values for both 0-TM and 1-TM_{di-vac} hops range from ~ 70 to 200 meV, with their mean values centered at ~ 130 meV. The fact that the migration barrier of some 1-TM_{di-vac} hop is comparable to that of 0-TM hops may be related to the ability of the face-sharing vanadium to relax away from the center of its octahedron. (20) This effect, especially pronounced for ions with d^0 electron configuration like V^{5+} (59,60), reduces the electrostatic repulsion between Li^+ in the tetrahedral site and the face-sharing V. This relatively low energy of tetrahedral Li-V face-sharing (20) is consistent with these features being observed in the equilibrium modeling of both $\text{Li}_{2-x}\text{VO}_3$ (30) and $\text{Li}_{3+x}\text{V}_2\text{O}_5$ DRX materials. (20) As there is no significant difference between 0-TM and 1-TM_{di-vac} hops, we used a single KRA value for the KMC simulation to further simplify the kinetic model. The energy difference between the initial and final states of the hop, captured by the CE, accounts for the difference between the migration barriers for 0-TM and 1-TM_{di-vac} hops. Using a single KRA value for parametrizing the energy barrier of Li^+ hops has been successfully employed in other transport studies based on KMC simulations. (23) The selected KRA value for any octahedral-to-tetrahedral (or vice versa) hop is set at 200 meV, equal to the upper limit of the KRA values presented in Figure 2. Utilizing a single KRA value can influence the absolute magnitude of Li^+ diffusivity, which we further elaborate on in the discussion section.

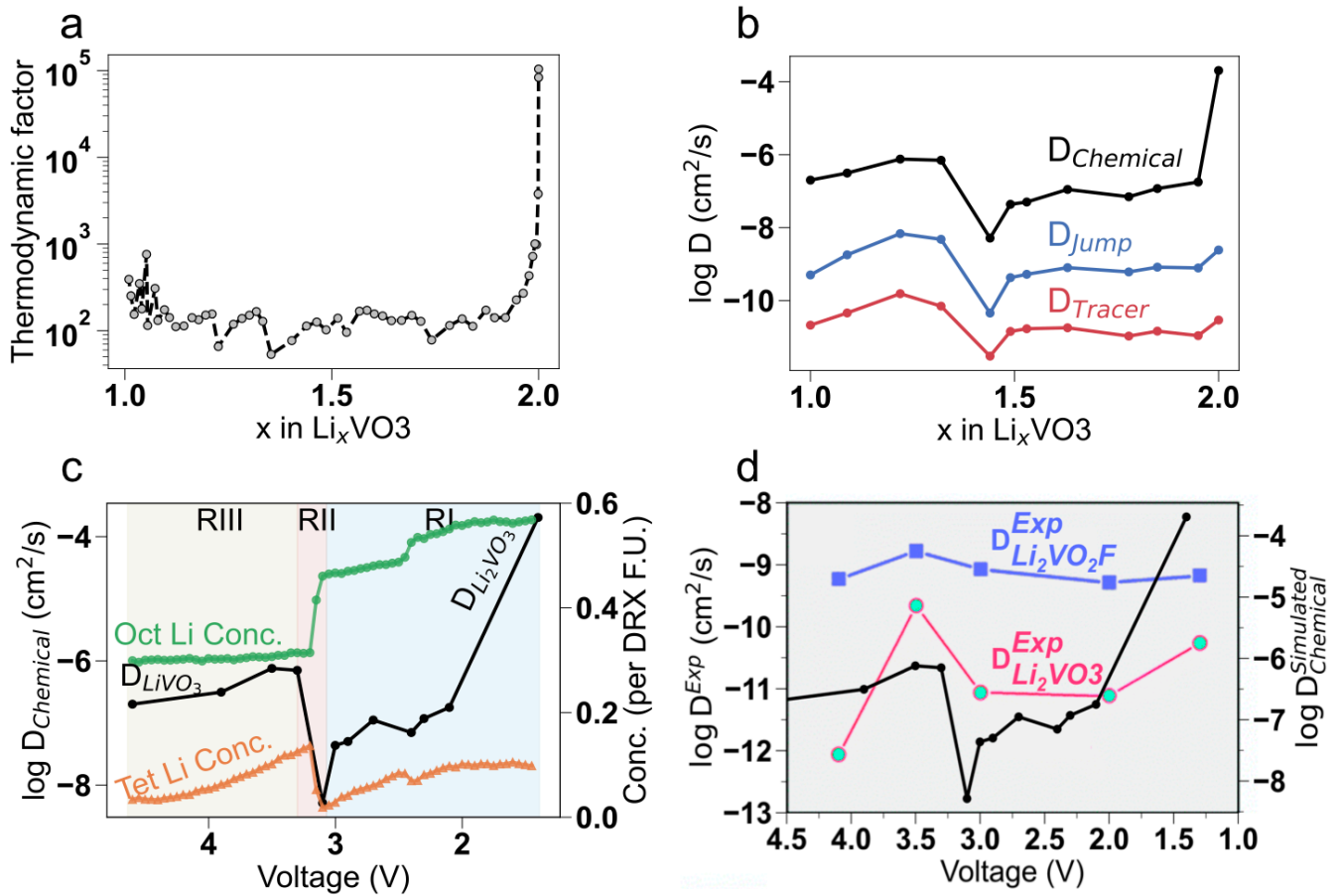


FIG. 3. (a) The calculated thermodynamic factor, Θ , is shown as a function of Li content, x , in Li_xVO_3 , at 300 K. The thermodynamic factor diverges at $x_{\text{Li}} = 2$, corresponding to the fully lithiated composition. (b) The calculated D_{Tracer} (red), D_{Jump} (blue), and D_{Chemical} (black) are displayed as a function of the Li content in Li_xVO_3 at 300 K, in units of cm^2/s . (c) The computed concentrations of octahedral Li (green) (30), tetrahedral Li (orange) (30), and D_{Chemical} (black) as a function of voltage (30). The regions RI, RII, and RIII correspond to the voltage ranges of (1.4 to 3.1), (3.1 to 3.3), and (3.3 to 4.6), respectively. (d) Experimental diffusivity of Li_2VO_3 (red curve) and $\text{Li}_2\text{VO}_2\text{F}$ (blue curve) obtained by Chen et al. (24) and simulated diffusivity of Li_2VO_3 (black curve) calculated by KMC simulations.

Figure 3a displays the thermodynamic factor calculated at 300 K as a function of Li content in Li_xVO_3 . The value of the thermodynamic factor is on the order of 10^2 but diverges to much larger values for the fully lithiated composition as the thermodynamic factor is proportional to the inverse of the vacancy concentration. (6,22,47) Such behavior of the thermodynamic factor has been previously observed in certain layered and spinel systems. (6,22,47)

Figure 3b displays D_{Chemical} (black), D_{Jump} (blue), and D_{Tracer} (red) calculated using equations 2, 4, and 5 as a function of Li content in Li_xVO_3 . The magnitude of D_{Tracer} ranges from 10^{-11} to 10^{-10} cm^2/s , whereas that of D_{Jump} spans from 10^{-10} to 10^{-8} cm^2/s . In contrast, the magnitude of D_{Chemical} mainly falls between 10^{-8} and 10^{-6} cm^2/s , except at the fully lithiated state, where it is on the order of 10^{-4} cm^2/s . Consistent with other kinetic studies on certain layered and spinel systems, D_{Tracer} is the lowest among the diffusion coefficients. (6,22,47) This finding occurs because D_{Jump} and D_{Chemical} rely on the collective displacements of Li^+ rather

than the average displacements of individual ions, which is the case for D_{Tracer} .

A noticeable jump in all the simulated diffusion coefficients is observed, with the lowest point occurring at the $\text{Li}_{1.44}\text{VO}_3$ composition and the highest point at $\text{Li}_{1.22}\text{VO}_3$. To investigate the reason for this jump, we present the concentrations of octahedral Li (green) (30) and tetrahedral Li (orange) (30) and the corresponding D_{Chemical} as a function of voltage (30) in Figure 3c. In order to directly compare the simulated diffusivity with the experimental diffusivity of Li_2VO_3 (red curve in Figure 3d) obtained by Chen et al. (24), we analyze these quantities as a function of voltage instead of Li concentration in both Figure 3c and 3d.

Figure 3c highlights three regions. Region I (RI), which covers the voltage range of (1.4 to 3.1), corresponds to the delithiation of Li_2VO_3 down to $\text{Li}_{1.49}\text{VO}_3$ (as shown in Figure 3b). In this region, the magnitude of D_{Chemical} initially decreases from Li_2VO_3 to $\text{Li}_{1.95}\text{VO}_3$ and then remains approximately constant at $\sim 10^{-7}$ cm^2/s . The experimental diffusivity of this material exhibits a similar change as a function of voltage within this voltage range, as shown in Figure 3d. (24) Additionally, we observe that both the

tetrahedral and octahedral Li concentrations decrease in this voltage range.

Region II (RII), covering the voltage range of (3.1 to 3.3), corresponds to the delithiation of $\text{Li}_{1.49}\text{VO}_3$ to $\text{Li}_{1.32}\text{VO}_3$. As depicted in Figure 3c, we observe an increase in diffusivity along with the concentration of tetrahedral Li while the concentration of octahedral Li decreases. The experimental diffusivity of this material exhibits a similar jump within the similar voltage window. (24) The simultaneous decrease/increase in the octahedral/tetrahedral Li concentration suggests that some of the octahedral Li migrates to the tetrahedral sites. (30) This migration has also been observed for the fluorinated iso-structure of this material at this composition, $\text{Li}_{1.44}\text{VO}_2\text{F}$. (61) Such collective migration phenomena are known to occur in ordered spinel compounds (62); however, they have not yet been well characterized for cation-disordered materials. This correlation between the magnitude of diffusivity as a function of Li content and the

concentrations of Li in tetrahedral and octahedral sites underscores the importance of considering both tetrahedral and octahedral sites in the transport analysis of DRX materials.

Region III (RIII) spans the voltage range of (3.3 to 4.6) and corresponds to the delithiation of $\text{Li}_{1.32}\text{VO}_3$ to LiVO_3 . In this region, we observe a decrease in diffusivity, which aligns with the behavior of the experimental diffusivity of Li_xVO_3 as a function of voltage. (24) In RIII, the Li concentration in octahedral sites remains constant while the tetrahedral Li concentration decreases. This suggests that Li extraction from $\text{Li}_{1.44}\text{VO}_3$ primarily occurs from high-voltage tetrahedral sites (30), contributing to the lower diffusivity in this range. Notably, the experimental diffusivity of this material decreases more rapidly (24) than the simulated diffusivity in RIII. In the discussion section, we use our understanding derived from the Li_2VO_3 compound to help interpret the experimental diffusion behaviors of $\text{Li}_2\text{VO}_2\text{F}$.

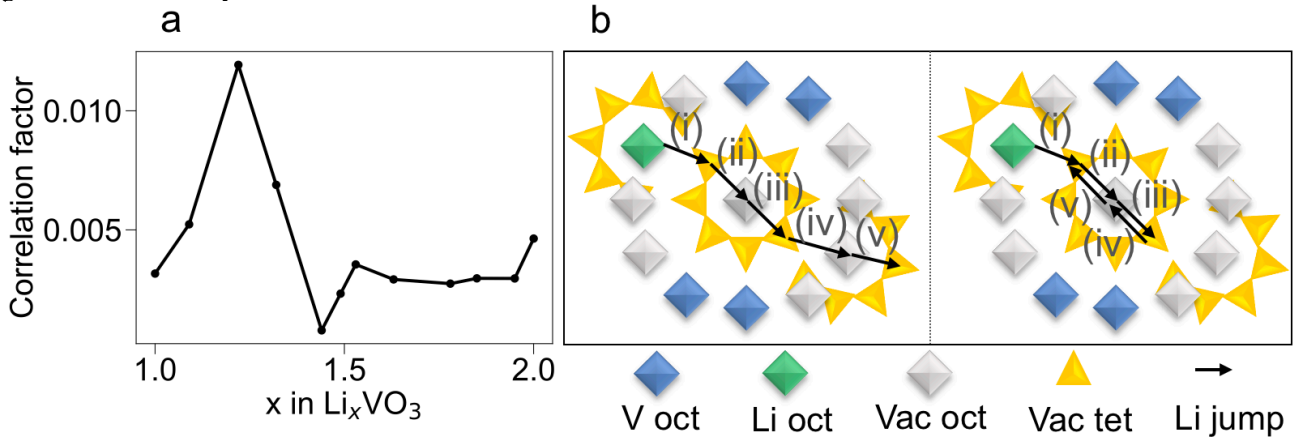


FIG. 4. (a) The calculated correlation factor as a function of Li content, x , in Li_xVO_3 . (b) A two-dimensional schematic of a Li-ion migrating in a rocksalt structure is shown. The left panel represents the case where the correlated motion of Li-ions is not considered, whereas the right panel represents the case where the correlated motion is included. In a rocksalt structure, each octahedral site (shown with diamonds) edge-shares with 12 other octahedral sites and face-shares with 8 tetrahedral sites (shown with triangles). The V-ions are represented by blue diamonds, while the green diamonds, gray diamonds, and yellow triangles represent octahedral Li sites, octahedral vacant sites, and tetrahedral vacant sites, respectively. The black arrows denote the Li^+ jumps, which are labeled sequentially from (i) to (v).

Figure 4a displays the calculated correlation factor plotted against the Li content in Li_xVO_3 . The correlation factor ranges between 10^{-3} and 10^{-2} with the highest value at the composition $\text{Li}_{1.22}\text{VO}_3$ and the lowest value at $\text{Li}_{1.44}\text{VO}_3$. The observed correlation factor in Li_xVO_3 is consistent with the predicted range of 10^{-3} to 10^{-2} in the DRX transport model developed by Anand et al. (63) For comparison, the correlation factor for diffusion in layered LiCoO_2 (6) and the spinels $\text{Li}_{1+x}\text{Ti}_2\text{O}_4$ (47) and Li_xTiS_2 (22) is on the order of 10^{-1} across varying Li content, while the predicted correlation factor for Mg_xTiS_2 (23) can be as low as 10^{-5} . Unlike Li_xCoO_2 (6) and the spinels Mg_xTiS_2 (23), Na_xTiS_2 (23), Li_xTiS_2 (23), which show an increase in the correlation factor with delithiation (i.e., increasing vacancy concentration), the correlation factor of DRX Li_xVO_3 does not show a consistent trend with increasing vacancy concentration. This finding indicates that factors other than the vacancy concentration

play a role in determining Li^+ correlated motion in this DRX system.

To enhance our understanding of Li^+ correlated motion, Figure 4b depicts how Li-ions move in a local environment based on the results of the KMC simulation. The left panel of Figure 4b shows Li^+ migration from one octahedral site to another without significant self-correlation. However, in systems in which there is significant correlation, Li^+ hops back and forth between specific sites, slowing its progress to the following site, as depicted in the right panel of Figure 4b. This type of correlated motion is commonly observed and has been extensively studied in ionic conductors and electrolytes (64–66) and is known as *self-correlated* motion, reflected in the D_{Tracer} value. (67)

It has been mathematically demonstrated that the connectivity of the sites impacts the correlated motion. (67) The connectivity of the sites can be disrupted if a high-barrier channel obstructs a network. In such cases, migrating Li^+ cannot move past the block or percolate through the structure.

(4,5) Both Li-excess and cation short-range ordering influence the formation of a percolating network in DRX. (11,33,68,69) As previously mentioned, Li-excess results in the formation of Li_4 clusters, whereas cation short-range ordering determines the extent of Li_4 tetrahedral connectivity in DRX materials. (11,33,68,69) Another factor responsible for the correlated motion is the ionic interactions that introduce non-uniformity in the energy landscape. (67) When an ion jumps uphill it is now more likely to jump backward to the site it came from. As stated by Anand et al. (63), when the standard deviation of the site-energy distribution exceeds $k_B T$, the fraction of Li sites involved in percolation can be significantly lower (63) than what the 0-TM percolation theory predicts. (4,5) It is worth noting that the model developed by Anand et al. represents Li-TM and Li-Li interactions through variations in site energies, considering all sites as Li/vacancy sites. (63)

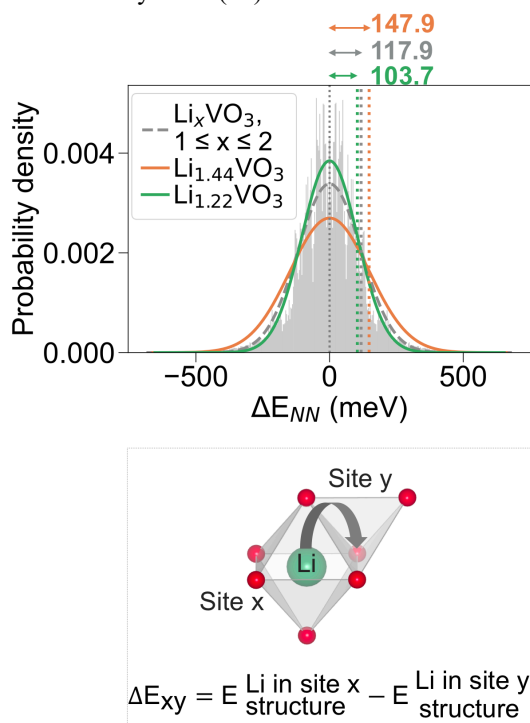


FIG. 5. The gray histogram in the above panel illustrates the energy difference between nearest-neighbor sites (ΔE_{NN}) along the hops in the kinetic Monte Carlo simulation in the composition range of Li_xVO_3 ($1 \leq x \leq 2$). The dotted gray curve represents the fitted normal distribution to this histogram. The orange and green curves correspond to the normal distribution curves fitted to the energy differences between nearest-neighbor sites along the Li^+ hops restricted to compositions $\text{Li}_{1.44}\text{VO}_3$ and $\text{Li}_{1.22}\text{VO}_3$, respectively. The values 103.7, 117.9, and 147.9 at the top of the plot indicate the standard deviations of ΔE_{NN} for compositions $\text{Li}_{1.22}\text{VO}_3$, Li_xVO_3 ($1 \leq x \leq 2$), and $\text{Li}_{1.44}\text{VO}_3$, respectively. The schematic on the bottom further clarifies the meaning of ΔE_{NN} along the hop.

Figure 5 presents the energy difference between the nearest-neighbor sites along the Li^+ hop (ΔE_{NN}). The gray histogram in the background of Figure 5 illustrates the distribution of ΔE_{NN} within the composition range of Li_xVO_3 ($1 \leq x \leq 2$). The dotted gray curve represents the normal distribution fitted to the ΔE_{NN} histogram and shows a standard deviation of approximately 118 meV. When fitted to only

energy differences that occur at composition $\text{Li}_{1.22}\text{VO}_3$ (green) the distribution narrows to 104 meV, while at composition $\text{Li}_{1.44}\text{VO}_3$ (orange) the distribution widens to 148 meV. Comparison of these hop distributions with the correlation factor in Figure 4a suggests that flatter energy landscapes, characterized by a narrower hop energy distribution, increase the correlation factor and thereby the effective diffusivity, as suggested by Anand. (63)

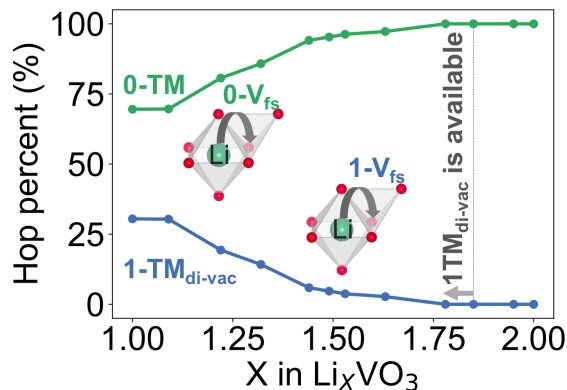


FIG. 6. The percentage of Li^+ hops from octahedral to tetrahedral sites that face-share with no vanadium (0-TM) (represented in green) or with one vanadium (depicted in blue) as function of Li composition.

The initial premise of the 0-TM percolation theory underscored the significance of incorporating 0-TM in transport analysis. (4,5) Our KMC model provides the opportunity to investigate the environment through which Li ions hop. We present in Figure 6 the percentage of hops from octahedral to 0-TM and 1-TM_{di-vac} tetrahedral sites. Our results reveal a consistent predominance of Li^+ hops from octahedral to 0-TM tetrahedral sites over those to 1-TM_{di-vac} tetrahedral sites, consistent with the basic idea of 0-TM percolation theory. (4,5) The lack of availability of 1-TM_{di-vac} at high Li content is not unexpected, considering prior work on LiCoO_2 in which it was observed that the divacancy mechanism only becomes accessible for $x_{\text{Li}} < 0.8$. (6)

Our analysis proposes that as the number of vacancies increases towards $x_{\text{Li}} = 1$, hops to a tetrahedral site with face-sharing vanadium (1-TM_{di-vac}) occur, but remain minority pathways. Although our analysis has been centered on octahedral-to-tetrahedral hops rather than octahedral-tetrahedral-octahedral hops, our findings confirm that as a general rule 0-TM channels do provide the pathway for Li percolation though extensions to include the 1-TM_{di-vac} mechanism could be relevant near the top of charge.

DISCUSSION

In this paper we investigated the macroscopic diffusion mechanism in the disordered rocksalt Li_xVO_3 by combining a cluster expansion for the energy landscape and limited migration hops from octahedral to tetrahedral sites and vice versa. The incorporation of the tetrahedral site as a distinct lithium site enables us to better understand the role it plays in delithiation and its kinetics. Specifically, Figure 3c demonstrates the significant impact of the relative stability

between Li in tetrahedral and octahedral sites on the variation of Li^+ diffusivity with Li content.

In contrast to certain layered and spinel systems (6,22,23,47), the diffusion coefficient (Figure 3b) and correlation factor (Figure 4a) of Li_xVO_3 do not improve with an increasing vacancy concentration. Moreover, empirical evidence shows that the diffusivity of DRX materials (11,12,17,24) remains relatively stable even when the Li concentration varies. This indicates the presence of other influential factors that overshadow the effect of vacancy concentration. The distribution of the Li site energy in DRX structures is greatly affected by the variation in the number and chemistry of the surrounding TM around the Li sites, which is determined by the strength of the Li-TM interaction. (19) For Li^+ to percolate efficiently, there must be a network of low-barrier local environments where all the nearest-neighbor sites are in a similar energy range. (63,66) Notably, the importance of the energy landscape in the kinetics of DRX materials is highlighted by Figure 5 and the recent publication by Anand et al. (63) For ordered layered structures such as LiCoO_2 , where all the Li sites have the same number of TM around them, overcoming the energy difference between the initial and final states of the hop is not a significant issue, as the only difference is in the vacancy concentration. (6) However, Figure 5 reveals that for DRX Li_xVO_3 , even the composition with highest diffusivity ($\text{Li}_{1.22}\text{VO}_3$) can exhibit a difference in nearest-neighbor site energies exceeding 400 meV. This substantial variation in nearest-neighbor site energy within Li_xVO_3 can help to explain the low correlation factor in Li_xVO_3 comparing to some layered and spinel systems. (6,22,23)

Our results reveal that the abrupt enhancement in both theoretical and experimental diffusivity shown in Figure 3d, (24) between the compositions of $\text{Li}_{1.22}\text{VO}_3$ ($V = 3.5$ V) and $\text{Li}_{1.44}\text{VO}_3$ ($V = 3.1$ V), can be attributed to the somewhat sudden transition of Li^+ from octahedral to tetrahedral sites, as demonstrated in Figure 3c. This same transition from octahedral to tetrahedral Li^+ migration has been computationally observed in $\text{Li}_{1.44}\text{VO}_2\text{F}$, a fluorinated isostructural counterpart of Li_2VO_3 . (61) Interestingly, the experimental diffusivity of $\text{Li}_2\text{VO}_2\text{F}$ (shown in Figure 3d) (24) exhibits a jump at 3.5 V ($\sim \text{Li}_{1.44}$) (24), similar to the theoretical and experimental findings observed in the oxide compound, though with a less pronounced peak. (24) Collective migration phenomena such as these are recognized in ordered spinel compounds (62), yet their occurrence within DRX compounds is somewhat surprising. A potential explanation for this collective motion could be that following the removal of 28% of Li (from Li_2VO_3 to $\text{Li}_{1.44}\text{VO}_3$), the energy for Li to occupy tetrahedral and octahedral sites begins to converge due to the creation of vacancies on octahedral sites (which lower the energy of tetrahedral occupancy). Support for this explanation is provided in Figure 5, where the distribution of hop energies in the $\text{Li}_{1.22}\text{VO}_3$ composition exhibits the smallest standard deviation, indicating a dense network of available sites with comparable energies. Consequently, the correlation factor and the diffusion

coefficient increase from $\text{Li}_{1.44}\text{VO}_3$, peaking at the composition $\text{Li}_{1.22}\text{VO}_3$.

An increase in the stability of Li^+ in tetrahedral sites can enhance the diffusivity by providing more available sites for Li^+ ; however, when the site energy for Li in tetrahedral sites becomes too low, their occupation by Li^+ can also impede migration through these sites, leading to lower experimental (24) and theoretical diffusivities as observed in highly delithiated states. Notably, the experimental diffusivity of Li_xVO_3 (24) declines more rapidly near the end of the charge than the theoretical diffusivity.

The experimental diffusivity of Li_2VO_3 has been reported to fall in the range of 10^{-12} to 10^{-10} cm^2/s (Figure 3d) (24), which is around four orders of magnitude lower than our simulated chemical diffusivity. Other kinetic studies have also observed this disparity between the experimental and computed diffusivity. (23,65) This discrepancy may have multiple origins. One of the primary problems when comparing experimental and simulated diffusivities is the challenge in estimating the active electrode and electrolyte surface area. (22) In the past, everything from the active electrode area to the total particle surface area has been used leading to very different diffusion constants. Assumptions in the theory models, such as the choice of single KRA and prefactor values, the diffusion mechanisms considered, may also contribute to the deviation between the experimental and theoretical diffusivity, though it seems unlikely that these would lead to variations that are more than an order of magnitude. The lack of any consideration of electronic transport limitations, either at the particle or electrode level may further complicate comparison between theory and experiment. Consequently, kinetic studies, including ours, have primarily concentrated on how the diffusivity varies with Li content rather than focusing on its absolute magnitude. (23)

The probability of finding tetrahedral sites in $\text{Li}_{2-x}\text{VO}_3$ face-sharing with 1-V, is twice as high as the probability of tetrahedral sites without face-sharing, as illustrated in Figure S3. Nevertheless, Figure 6 demonstrates that nearly all octahedral-to-tetrahedral hops within the composition range of $\text{Li}_{1.63}\text{VO}_3$ to Li_2VO_3 are into tetrahedral sites without V face-sharing. Beginning with the composition $\text{Li}_{1.32}\text{VO}_3$, we observe that over 10% of hops are to 1-TM_{di-vac} tetrahedral sites, and this fraction rises to approximately 25% for LiVO_3 . Still, our findings indicate that the substantial energy difference between octahedral and 1-TM tetrahedral sites makes the 0-TM network the most relevant pathway for Li^+ transport in DRX materials.

This study, along with the one conducted by Anand et al. (63), supports the notion that a flat energy landscape improves effective Li^+ percolation in DRX structures. However, no established strategy exists for creating a flat energy landscape in such structures. A study on the $\text{Li}_2\text{VO}_2\text{F}$ compound demonstrated that substituting some of the V with Fe or Ti can enhance the electrochemical cyclability and reduce the voltage slope (70), suggesting a flatter energy landscape. Research on high-entropy disordered cathodes (71) has

indicated that using a variety of TMs can decrease short-range order and promote long-range Li⁺ transport. (71) Although introducing multiple TMs reduces short-range ordering (71), further investigation is needed to understand how this reduction influences the site energy distribution and whether it improves Li⁺ transport properties by flattening the energy landscape or if other factors contribute to the enhancement.

The positive impact of F on Li⁺ transport has also been demonstrated in other studies. (33) Comparing the experimental diffusivity of Li₂VO₃ and Li₂VO₂F (Figure 3d) (24) further emphasizes the advantages of F, as the fluorinated compound exhibits a diffusivity of approximately 1 to 3 orders of magnitude higher than that of the oxide compound. However, the amount of F must be carefully selected, as F can also immobilize Li due to strong Li–F bonds when a high concentration of vacancies is present. (69)

Due to the complexity of Li⁺ transport in the DRX materials, accurately predicting Li⁺ transport properties requires information on the site energy distribution and interactions, which can be obtained through advanced modeling techniques such as the CE and KMC simulations employed in this work. Our findings emphasize the importance of understanding the factors contributing to a flat energy landscape in DRX materials. More precise results will be achieved if the comparison of Li⁺ percolation across different DRX materials is based on both 0-TM connectivity network as well as their energy landscape.

CONCLUSION

In this study, we used KMC simulations to examine the kinetics of Li⁺ transport in a Li₂VO₃ DRX material. Our findings underscore the necessity of considering the Li occupancy in both tetrahedral and octahedral sites to understand any potential collective ion migration and its possible impact on the macroscopic diffusivity. Our results show that the diffusivity and correlation factor of Li_xVO₃ do not exhibit enhancement as the vacancy concentration increases, which contrasts with the patterns observed in kinetic studies of some layered and spinel systems. This observation suggests that an uneven energy landscape within the DRX structures, can outweigh the influence of vacancy concentrations. Our findings continue to demonstrate that while 1-TM_{di-vac} channels play a role in the diffusion process, it is the 0-TM channels that remain the primary channels, especially in highly lithiated states where the vacancy concentration is insufficient to activate the 1-TM_{di-vac} mechanism.

ACKNOWLEDGMENTS

This work was supported by the Assistant Secretary for Energy Efficiency and Renewable Energy, Vehicle Technologies Office, under the Applied Battery Materials Program, of the U.S. Department of Energy under contract no. DE-AC02-05CH11231. The computational analysis was performed using computational resources sponsored by the Department of Energy's Office of Energy Efficiency and Renewable Energy and located at the National Renewable

Energy Laboratory as well as computational resources provided by Extreme Science and Engineering Discovery Environment (XSEDE), supported by the National Science Foundation grant number ACI1053575, and the National Energy Research Scientific Computing Center (NERSC), a DOE Office of Science User Facility supported by the Office of Science and the U.S. Department of Energy under contract no. DE-AC02-05CH11231. ZJ, LBL, and TC acknowledge financial support from the NSF Graduate Research Fellowship Program (GRFP) under contract no. DGE 1752814, DGE 1752814, and DGE 1106400, respectively. Any opinions, findings, conclusions, or recommendations expressed in this material are those of the author(s) and do not necessarily reflect the views of the National Science Foundation.

REFERENCES

1. Delmas C, Br ethes S, M en etrier M. ω -Li_xV₂O₅ — a new electrode material for rechargeable lithium batteries. *J Power Sources*. 1991 Mar 1;34(2):113–8.
2. Obrovac MN, Mao O, Dahn JR. Structure and electrochemistry of LiMO₂ (M=Ti, Mn, Fe, Co, Ni) prepared by mechanochemical synthesis. *Solid State Ion*. 1998 Sep 2;112(1):9–19.
3. Cl ement RJ, Lun Z, Ceder G. Cation-disordered rocksalt transition metal oxides and oxyfluorides for high energy lithium-ion cathodes. *Energy Environ Sci*. 2020;13(2):345–73.
4. Lee J, Urban A, Li X, Su D, Hautier G, Ceder G. Unlocking the Potential of Cation-Disordered Oxides for Rechargeable Lithium Batteries. *Science*. 2014 Jan 31;343(6170):519–22.
5. Urban A, Lee J, Ceder G. The Configurational Space of Rocksalt-Type Oxides for High-Capacity Lithium Battery Electrodes. *Adv Energy Mater*. 2014;4(13):1400478.
6. Van der Ven A, Ceder G, Asta M, Tepesch PD. First-principles theory of ionic diffusion with nondilute carriers. *Phys Rev B*. 2001 Oct 25;64(18):184307.
7. Lee J, Kitchaev DA, Kwon DH, Lee CW, Papp JK, Liu YS, et al. Reversible Mn²⁺/Mn⁴⁺ double redox in lithium-excess cathode materials. *Nature*. 2018 Apr;556(7700):185–90.
8. Chen R, Ren S, Knapp M, Wang D, Witter R, Fichtner M, et al. Disordered Lithium-Rich Oxyfluoride as a Stable Host for Enhanced Li⁺ Intercalation Storage. *Adv Energy Mater*. 2015;5(9):1401814.
9. Yabuuchi N, Takeuchi M, Nakayama M, Shiiba H, Ogawa M, Nakayama K, et al. High-capacity electrode materials for rechargeable lithium batteries: Li₃NbO₄-based system with cation-disordered rocksalt structure. *Proc Natl Acad Sci*. 2015;112(25):7650–5.
10. Ren S, Chen R, Maawad E, Dolotko O, Guda AA, Shapovalov V, et al. Improved Voltage and Cycling for Li⁺ Intercalation in High-Capacity Disordered Oxyfluoride Cathodes. *Adv Sci*. 2015;2(10):1500128.
11. Ji H, Urban A, Kitchaev DA, Kwon DH, Artrith N, Ophus C, et al. Hidden structural and chemical order controls lithium transport in cation-disordered oxides for rechargeable batteries. *Nat Commun*. 2019;10(1):592.
12. Lee J, Wang C, Malik R, Dong Y, Huang Y, Seo DH, et al. Determining the Criticality of Li-Excess for Disordered-Rocksalt Li-Ion Battery Cathodes. *Adv Energy Mater*. 2021;11(24):2100204.
13. A. House R, Jin L, Maitra U, Tsuruta K, W. Somerville J, P. F orstermann D, et al. Lithium manganese oxyfluoride as a new cathode material exhibiting oxygen redox. *Energy Environ Sci*. 2018;11(4):926–32.
14. Yabuuchi N, Nakayama M, Takeuchi M, Komaba S, Hashimoto Y, Mukai T, et al. Origin of stabilization and destabilization in solid-state redox reaction of oxide ions for lithium-ion batteries. *Nat Commun*. 2016 Dec;7(1):13814.
15. Kitchaev DA, Lun Z, Richards WD, Ji H, Cl ement RJ, Balasubramanian M, et al. Design principles for high transition metal capacity in disordered rocksalt Li-ion cathodes. *Energy Environ Sci*. 2018;11(8):2159–71.

16. Zhang H, Gao X, Cai Q, Zhang X, Tian Y, Jia M, et al. Recent progress and perspectives on cation disordered rock-salt material for advanced Li-ion batteries. *J Mater Chem A*. 2023;11(16):8426–52.
17. Huang J, Zhong P, Ha Y, Kwon DH, Crafton MJ, Tian Y, et al. Non-topotactic reactions enable high rate capability in Li-rich cathode materials. *Nat Energy*. 2021 Jul;6(7):706–14.
18. Wang X, Huang Y, Ji D, Omenya F, Karki K, Sallis S, et al. Structure evolution and thermal stability of high-energy-density Li-ion battery cathode Li₂VO₂F. *J Electrochem Soc*. 2017;164(7):A1552.
19. Abdellahi A, Urban A, Dacek S, Ceder G. Understanding the effect of cation disorder on the voltage profile of lithium transition-metal oxides. *Chem Mater*. 2016;28(15):5373–83.
20. Guo X, Chen C, Ong SP. The Intercalation Chemistry of the Disordered RockSalt Li₃V₂O₅ Anode from Cluster Expansions and Machine Learning Interatomic Potentials [Internet]. arXiv; 2022 [cited 2022 Sep 8]. Available from: <http://arxiv.org/abs/2208.14420>
21. Liu H, Zhu Z, Yan Q, Yu S, He X, Chen Y, et al. A disordered rock salt anode for fast-charging lithium-ion batteries. *Nature*. 2020 Sep 3;585(7823):63–7.
22. Bhattacharya J, Van der Ven A. First-principles study of competing mechanisms of nondilute Li diffusion in spinel Li_xTi₅S₂. *Phys Rev B*. 2011 Apr 18;83(14):144302.
23. Kolli SK, Van der Ven A. Elucidating the Factors That Cause Cation Diffusion Shutdown in Spinel-Based Electrodes. *Chem Mater*. 2021 Aug 24;33(16):6421–32.
24. Chen R, Ren S, Yavuz M, Guda AA, Shapovalov V, Witter R, et al. Li⁺ intercalation in isostructural Li₂VO₃ and Li₂VO₂F with O²⁻ and mixed O²⁻/F⁻ anions. *Phys Chem Chem Phys*. 2015 Jun 24;17(26):17288–95.
25. Andersen M, Panosetti C, Reuter K. A Practical Guide to Surface Kinetic Monte Carlo Simulations. *Front Chem* [Internet]. 2019 [cited 2023 Jan 25];7. Available from: <https://www.frontiersin.org/articles/10.3389/fchem.2019.00202>
26. Sanchez JM, Ducastelle F, Gratias D. Generalized cluster description of multicomponent systems. *Phys Stat Mech Its Appl*. 1984;128(1–2):334–50.
27. De Fontaine D. Cluster approach to order-disorder transformations in alloys. *Solid State Phys*. 1994;47:33–176.
28. Laks DB, Ferreira LG, Froyen S, Zunger A. Efficient cluster expansion for substitutional systems. *Phys Rev B*. 1992 Nov 15;46(19):12587–605.
29. Barroso-Luque L, Yang JH, Xie F, Chen T, Kam RL, Jadidi Z, et al. smol: A Python package for cluster expansions and beyond. *J Open Source Softw*. 2022 Sep 29;7(77):4504.
30. Jadidi Z, Yang J, Chen T, Barroso-Luque L, Ceder G. Ab-initio study of short-range ordering in vanadium-based disordered rocksalt structures. *J Mater Chem A*. 2023; DOI: 10.1039/D3TA02475J
31. Van De Walle A. Multicomponent multisublattice alloys, nonconfigurational entropy and other additions to the Alloy Theoretic Automated Toolkit. *Calphad*. 2009;33(2):266–78.
32. Ceder G, Garbulsky GD, Tepeš PD. Convergent real-space cluster expansion for configurational disorder in ionic systems. *Phys Rev B*. 1995;51(17):11257.
33. Ouyang B, Artrith N, Lun Z, Jadidi Z, Kitchaev DA, Ji H, et al. Effect of Fluorination on Lithium Transport and Short-Range Order in Disordered-Rocksalt-Type Lithium-Ion Battery Cathodes. *Adv Energy Mater*. 2020;10(10):1903240.
34. Richards WD, Dacek ST, Kitchaev DA, Ceder G. Fluorination of lithium-excess transition metal oxide cathode materials. *Adv Energy Mater*. 2018;8(5):1701533.
35. Seko A, Tanaka I. Cluster expansion of multicomponent ionic systems with controlled accuracy: importance of long-range interactions in heterovalent ionic systems. *J Phys Condens Matter*. 2014;26(11):115403.
36. Hohenberg P, Kohn W. Inhomogeneous electron gas. *Phys Rev*. 1964;136:B864.
37. Kohn W, Sham LJ. Self-Consistent Equations Including Exchange and Correlation Effects. *Phys Rev*. 1965 Nov 15;140(4A):A1133–8.
38. Kresse G, Furthmüller J. Efficiency of ab-initio total energy calculations for metals and semiconductors using a plane-wave basis set. *Comput Mater Sci*. 1996 Jul 1;6(1):15–50.
39. Kresse G, Furthmüller J. Efficient iterative schemes for ab initio total-energy calculations using a plane-wave basis set. *Phys Rev B*. 1996 Oct 15;54(16):11169–86.
40. Kresse G, Joubert D. From ultrasoft pseudopotentials to the projector augmented-wave method. *Phys Rev B*. 1999;59(3):1758.
41. Blöchl PE. Projector augmented-wave method. *Phys Rev B*. 1994;50(24):17953.
42. Perdew JP, Burke K, Ernzerhof M. Generalized gradient approximation made simple. *Phys Rev Lett*. 1996;77(18):3865.
43. Wang L, Maxisch T, Ceder G. Oxidation energies of transition metal oxides within the GGA+U framework. *Phys Rev B*. 2006;73(19):195107.
44. Urban A, Seo DH, Ceder G. Computational understanding of Li-ion batteries. *Npj Comput Mater*. 2016;2(1):1–13.
45. Asari Y, Suwa Y, Hamada T. Formation and diffusion of vacancy-polaron complex in olivine-type LiMnPO₄ and LiFePO₄. *Phys Rev B*. 2011;84(13):134113.
46. Bruce PG, Lisowska-Oleksiak A, Saidi MY, Vincent CA. Vacancy diffusion in the intercalation electrode Li_{1-x}NiO₂. *Solid State Ion*. 1992 Oct 1;57(3):353–8.
47. Bhattacharya J, Van Der Ven A. Phase stability and nondilute Li diffusion in spinel Li_{1+x}Ti₂O₄. *Phys Rev B*. 2010 Mar 22;81(10):104304.
48. Van der Ven A, Bhattacharya J, Belak AA. Understanding Li Diffusion in Li-Intercalation Compounds. *Acc Chem Res*. 2013 May 21;46(5):1216–25.
49. Van Der Ven A, Thomas JC, Xu Q, Swoboda B, Morgan D. Nondilute diffusion from first principles: Li diffusion in Li_xTi₅S₂. *Phys Rev B*. 2008 Sep 26;78(10):104306.
50. Zwanzig R. Time-Correlation Functions and Transport Coefficients in Statistical Mechanics. *Annu Rev Phys Chem*. 1965;16(1):67–102.
51. Gomer R. Diffusion of adsorbates on metal surfaces. *Rep Prog Phys*. 1990 Jul;53(7):917–1002.
52. Zhou Y, Miller GH. Green-Kubo Formulas for Mutual Diffusion Coefficients in Multicomponent Systems. *J Phys Chem*. 1996 Jan 1;100(13):5516–24.
53. Aydinol MK, Kohan AF, Ceder G. Ab initio calculation of the intercalation voltage of lithium-transition-metal oxide electrodes for rechargeable batteries. *J Power Sources*. 1997 Oct 1;68(2):664–8.
54. Richards PM. Theory of one-dimensional hopping conductivity and diffusion. *Phys Rev B*. 1977 Aug 15;16(4):1393–409.
55. Mazenko G, Banavar JR, Gomer R. Diffusion coefficients and the time auto-correlation function of density fluctuations. *Surf Sci*. 1981 Jun 1;107(2):459–68.
56. Vineyard GH. Frequency factors and isotope effects in solid state rate processes. *J Phys Chem Solids*. 1957 Jan 1;3(1):121–7.
57. Bortz AB, Kalos MH, Lebowitz JL. A new algorithm for Monte Carlo simulation of Ising spin systems. *J Comput Phys*. 1975 Jan 1;17(1):10–8.
58. Bulnes FM, Pereyra VD, Riccardo JL. Collective surface diffusion: n-fold way kinetic Monte Carlo simulation. *Phys Rev E*. 1998;58(1):86.
59. Urban A, Abdellahi A, Dacek S, Artrith N, Ceder G. Electronic-structure origin of cation disorder in transition-metal oxides. *Phys Rev Lett*. 2017;119(17):176402.
60. Ok KM, Halasyamani PS, Casanova D, Llundell M, Alemany P, Alvarez S. Distortions in octahedrally coordinated d₀ transition metal oxides: A continuous symmetry measures approach. *Chem Mater*. 2006;18(14):3176–83.
61. Loftager S, Chang JH, Euchner H, Gross A, Baur C, Johnson R, et al. Novel Cathode Materials for Lithium Ion Batteries. [Internet]. Karlsruhe Institute of Technology; 2018 Sep. (LiRichFCC). Report No.: 711792. Available from: <https://ec.europa.eu/research/participants/documents/downloadPublic?documentIds=080166e5be07724f&appId=PPGMS>
62. Chen T, Yang J, Barroso-Luque L, Ceder G. Removing the Two-Phase Transition in Spinel LiMn₂O₄ through Cation Disorder. *ACS Energy Lett*. 2022 Dec 2;3:14–9.
63. Anand S, Chen T, Ceder G. Impact of the Energy Landscape on the Ionic Transport of Disordered Rocksalt Cathodes [Internet]. arXiv; 2023 [cited 2023 May 11]. Available from: <http://arxiv.org/abs/2301.10842>

64. Jacobson SH, Nitzan A, Ratner MA. Charge carrier correlations in framework solid electrolytes. *Solid State Ion.* 1981;5:125–8.
65. Xia H, Meng SY, Lu L, Ceder G. Electrochemical Behavior and Li Diffusion Study of LiCoO₂ Thin Film Electrodes Prepared by PLD. 2007;
66. Zeng Y, Ouyang B, Liu J, Byeon YW, Cai Z, Miara LJ, et al. High-entropy mechanism to boost ionic conductivity. *Science.* 2022;378(6626):1320–4.
67. Vargas-Barbosa NM, Roling B. Dynamic ion correlations in solid and liquid electrolytes: how do they affect charge and mass transport? *ChemElectroChem.* 2020;7(2):367–85.
68. Huang L, Zhong P, Ha Y, Cai Z, Byeon YW, Huang TY, et al. Optimizing Li-Excess Cation-Disordered Rocksalt Cathode Design Through Partial Li Deficiency. *Adv Energy Mater.* n/a(n/a):2202345.
69. Zhong P, Cai Z, Zhang Y, Giovine R, Ouyang B, Zeng G, et al. Increasing Capacity in Disordered Rocksalt Cathodes by Mg Doping. *Chem Mater.* 2020 Dec 22;32(24):10728–36.
70. Baur C, Källquist I, Chable J, Chang JH, Johnsen RE, Ruiz-Zepeda F, et al. Improved cycling stability in high-capacity Li-rich vanadium containing disordered rock salt oxyfluoride cathodes. *J Mater Chem A.* 2019;7(37):21244–53.
71. Lun Z, Ouyang B, Kwon DH, Ha Y, Foley EE, Huang TY, et al. Cation-disordered rocksalt-type high-entropy cathodes for Li-ion batteries. *Nat Mater.* 2021 Feb;20(2):214–21.

SUPPORTING INFORMATION

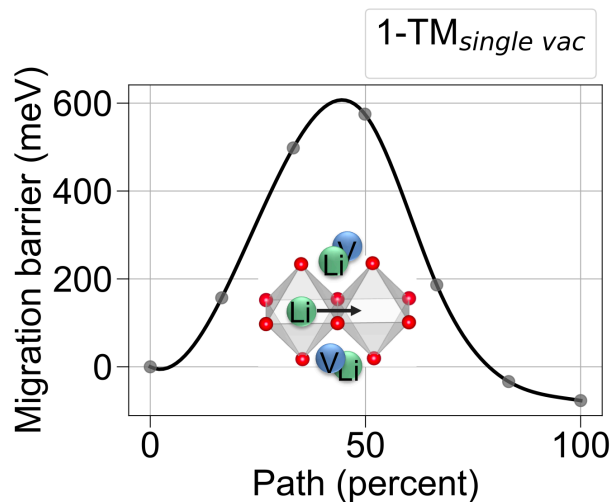


Figure S1: Energy (meV) along the Li migration pathway (%) for the octahedral-to-octahedral mechanism in Li_2VO_3 is examined when the lower and upper tetrahedral sites face-share with Li, V and one vacancy. Since the migration barrier exceeds 300 meV, it is safe to conclude that Li does not pass through the 1-TM single vacancy path. In addition, the intermediate tetrahedral site does not represent a local minimum in this case. Hence, we did not consider the 1-TM single vacancy hop in our KMC simulation.

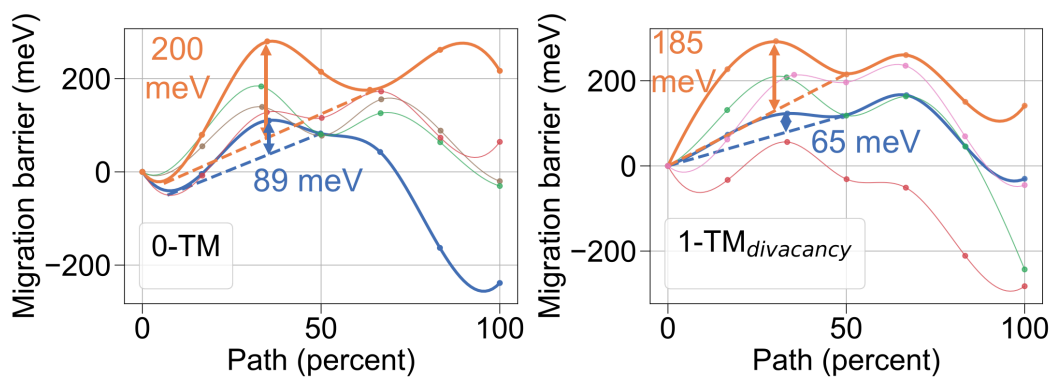


Figure S2: Energy (meV) along the Li migration pathway (%) for the octahedral-tetrahedral-octahedral mechanism in Li_xVO_3 ($1 \leq x \leq 2$): (left) when the tetrahedral site does not share a face with any V and (right) when it shares a face with one V and two octahedral vacancies. The minimum and maximum KRA values are indicated in each case.

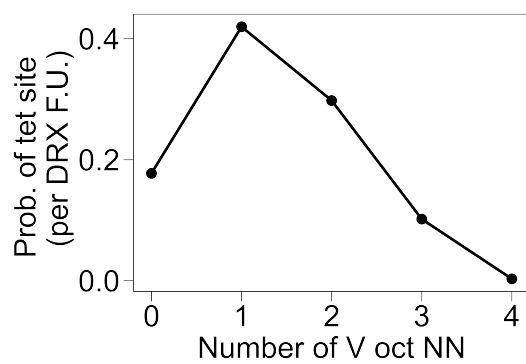


Figure S3: Probability of any tetrahedral site per DRX formula unit (F.U.) with a certain number of nearest-neighbor face-sharing V.